Accelerated freezing due to droplet pinning on a nanopillared surface

Cite as: AIP Advances 8, 125228 (2018); https://doi.org/10.1063/1.5048933 Submitted: 18 July 2018 . Accepted: 20 December 2018 . Published Online: 31 December 2018

Rachel Bohm, Mohammad Rejaul Haque 🗓, Chuang Qu, Edward C. Kinzel 🧓, and Amy Rachel Betz 🗓









ARTICLES YOU MAY BE INTERESTED IN

Spatial control of condensation and desublimation using ice nucleating proteins Applied Physics Letters 113, 153701 (2018); https://doi.org/10.1063/1.5046187

Droplet coalescence and freezing on hydrophilic, hydrophobic, and biphilic surfaces Applied Physics Letters 107, 141602 (2015); https://doi.org/10.1063/1.4932050

Numerical investigation of coalescence-induced self-propelled behavior of droplets on non-wetting surfaces

Physics of Fluids **30**, 112102 (2018); https://doi.org/10.1063/1.5046056







Accelerated freezing due to droplet pinning on a nanopillared surface

Rachel Bohm,¹ Mohammad Rejaul Haque,^{1,a} Chuang Qu,² Edward C. Kinzel,² and Amy Rachel Betz¹

¹Department of Mechanical and Nuclear Engineering, Kansas State University, Manhattan, Kansas 66506, United States

(Received 18 July 2018; accepted 20 December 2018; published online 31 December 2018)

The freezing process is significantly influenced by environmental factors and surface morphologies. At atmospheric pressure, a surface below the dew and freezing point temperature for a given relative humidity nucleates water droplets heterogeneously on the surface and then freezes. This paper examines the effect of nanostructured surfaces on the nucleation, growth, and subsequent freezing processes. Microsphere Photolithography (MPL) is used to pattern arrays of silica nanopillars. This technique uses a self-assembled lattice of microspheres to focus UV radiation to an array of photonic jets in photoresist. Silica is deposited using e-beam evaporation and liftoff. The samples were placed on a freezing stage at an atmospheric temperature of 22±0.5°C and relative humidities of 40% or 60%. The nanopillar surfaces had a significant effect on droplet dynamics and freezing behavior with freezing accelerated by an order of magnitude compared to a plain hydrophilic surface at 60% RH where the ice bridges need to cover a larger void for the propagation of the freezing front within the growing droplets. By pinning droplets, coalescence is suppressed for the nanopillared surface, altering the size distribution of droplets and accelerating the freezing process. The main mechanism affecting freezing characteristics was the pinning behavior of the nanopillared surface. © 2018 Author(s). All article content, except where otherwise noted, is licensed under a Creative Commons Attribution (CC BY) license (http://creativecommons.org/licenses/by/4.0/). https://doi.org/10.1063/1.5048933

Condensate freezing or frost is formed when a surface is cooled below the dew point and freezing temperature. At atmospheric pressure, water vapor from the air will first condense, then freeze on a cold surface. Both the droplet dynamics before freezing and the freezing propagation impact the total time until freezing¹ and the maximum freezing temperature.² Condensate freezing is of significant importance for applications such as aviation, satellites, power transmission, refrigeration, food preservation, and air conditioning. Engineered surfaces have the ability to control the droplet dynamics and freezing propagation.

Engineered surfaces such as hydrophobic, superhydrophobic, and biphilic surfaces have been previously tested as a method to delay or prevent freezing.^{3–15} Results are usually reported as the time delay until a surface is frozen^{1,3,6,7} or a temperature depression to freezing.² Freezing front propagation rates are also reported.^{8,12,16} Researchers also use active techniques to accelerate the freezing in food processing via ultrasound assisted freezing, high pressure freezing, pressure shift freezing, air-blast freezing etc.^{17–22} Hence, we believe that the present passive technique of accelerated freezing will reduce the daily power consumption in near future for the desirable applications such as food processes, agricultural processes, and freezing based desalination etc.

This work investigates the relationship between the "onset of freezing" and the "freezing front propagation rate". The propagation rate can also be expressed as the time difference between the



²Department of Mechanical and Aerospace Engineering, Missouri University of Science and Technology, Rolla, Missouri 065409, United States

^aAuthor to whom correspondence should be addressed. Electronic mail: mhaque@ksu.edu

onset of freezing and the total time until freezing.^{7,12} To elucidate frosting mechanisms, condensate freezing was studied on Microsphere Photolithography (MPL) created silica nanopillar (~0.7 µm pillar diameter and ~0.3µm pillar height in a 2 µm hexagonal close packed array) on a silicon substrate^{23–27} as shown in Fig. 1(a) and (b). An oxidized silicon wafer, referred to as the plain surface, was tested for the comparison. A Teflon© coated silicon surface was also tested. For an injected droplet, the apparent advancing and receding contact angle on plain and Teflon© coated surface was measured by tilt table method using goniometer (see supplementary material, Sec. I). The contact angle shows the different intrinsic wetting properties of the surfaces.

Nanopillared surfaces significantly accelerate freezing by pinning droplets, which impedes droplet mobility, coalescence, and growth. In order to prevent coalescence, the energy required to overcome the capillary pressure ($E_{capillary}$) must be higher than the surface energy reduction (E_s) by coalescing of droplets.²³ Based on certain assumptions, the minimum radius of the pillar required to pin the droplets can be the function of pillar height (h), and apparent contact angle (θ') of the condensed droplet. The fabricated pillar radius in present study is within the limit depicted by our previous work.²³ Hence, the designed nanopillars are expected to exhibit droplet pinning behavior. During the experiment, the pinned and irregularly shaped condensed droplets were observed. Directional anisotropy was also observed. A three-phase contact line ended along the edge of the pillar as shown in Fig. 1(c) and the bottom of the water droplet was not circular (black dotted line, inset). Hence, the condensed droplets were in Wenzel wetting state consistent to literature.^{23,28,29}

However, the accelerated freezing time, allows for the freezing dynamics to be observed many times under the same conditions. Furthermore, due to the random nature of droplet growth dynamics, the freezing times varies. The statistical variation of data produced allows for the exploration of the relationship between the droplet dynamics and freezing propagation.

The surface was placed on a cooling stage^{2,23} and the surface temperature was set to -8±0.5°C. The test set up (see supplementary material, Sec. II) was enclosed in an environmental chamber with an air temperature of 22±0.5°C and a relative humidity (RH) of 40% or 60%. The tests were conducted in the presence of non-condensable gases (air) at different RHs as RH can significantly

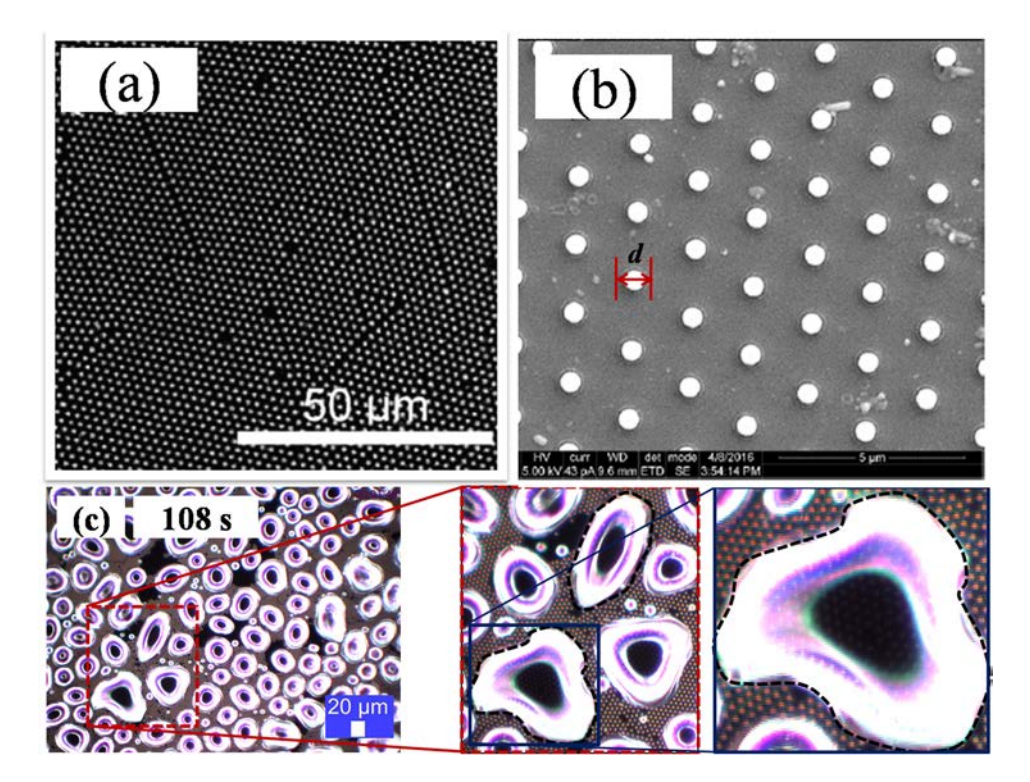


FIG. 1. (a) Microscopic image (b) SEM image (higher magnification) of the finished fabricated surface (c) wetting state of the condensed droplet (For contact angle, see supplementary material, Sec. I).

alter the nucleation energy barrier and nucleation site density. 30,31 For the nanopillared surfaces, more than 30 trials were recorded and analyzed for each relative humidity. For the plain and Teflon© coated surface, four trials were conducted. All the images and videos were captured focusing close to the center position of the sample (approximately 1 inch × 1 inch) by a Leica DVM2500 microscope at $600\times$, making the frame 383 microns by 510 microns. The videos were used to determine the freezing time. When drops froze on the nanopillared surfaces, there was very little change in the index of refraction or reflectance so that the pillars beneath the drops were visible through the ice nuclei (see supplementary material, Sec. IV).

At 40% RH the nanopillared droplet dynamics and freezing are notably different compared to the plain surface, as shown in Fig. 2 (see supplementary material, Sec. V). The droplets appear to be much smaller than the plain surfaces when the surfaces finish freezing. The droplets are consistently irregular in shape, and there is little visible ice bridging due to vapor pressure gradient over the two phases (water and ice). Additionally, the pinning of the droplets results in droplets very close together before coalescing. The droplets themselves are clear when they first freeze and the pattern is still visible through the droplets. They also do not appear to expand upon freezing compared to the plain surfaces. Freezing test has also been presented (Fig. 2e) for Teflon© coated silicon surface which delays the freezing even more compared to plain silicon surface (details, see supplementary material, Sec. VI). The recipe of the coating can be found from our previous work. Nanopillared surface accelerated freezing significantly compared to both of the control surfaces due to the unique pinning effect.

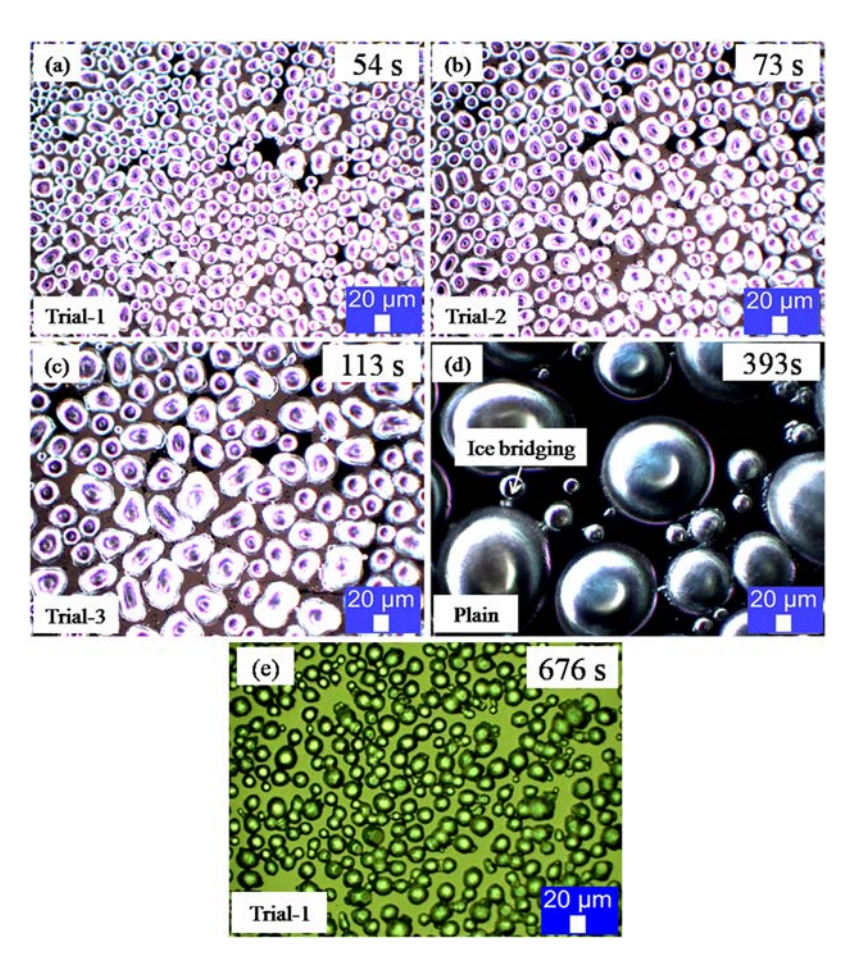


FIG. 2. Images taken when the surface fully freezes for 40% relative humidity (a) nanopillars frozen at 54 s, (b) nanopillars frozen at 73 s, (c) nanopillars frozen at 113 s, and (d) plain surface frozen at 393 s (e) Teflon© coated surface frozen at 676 s (35% RH). (a), (b), and (c) are different trials on the same nanopillared surface.

In addition, nanopillars create favorable conditions for the formation of amorphous ice, microcrystalline or cubic crystals. The process also creates transparent and cubic ice growth.³³ Hence, the lack of multidimensional dendritic growth³⁴ would have implications in HVAC systems, cryogenics, energy, and refrigeration applications.

As observed from Fig. 3, although droplet initial density seems quite similar at t=10 s, the different coalescence behavior due to pinning of the pillars, reduces droplet density significantly and eventually alters the size distribution of the droplet. Large sized droplet with lower droplet density (number of droplets per unit area) delays the freezing process. The higher the frequency of coalescence events, the longer the freezing delay, which is consistent to literature.²

Similar to the 40% RH condition, at 60% RH the nanopillared surface also freezes when the droplets are much smaller than the plain surface droplets (see supplementary material, Sec. VII for the detailed quantification). As seen in Fig. 4, the droplets at 60% RH are even more irregular in shape than the 40% RH pillars, and get even closer together without coalescing. There is no noticeable ice bridging for the nanopillared surfaces at 60% RH. The droplets are still transparent when frozen (which makes it harder to count) and do not expand much when frozen.

The plain surfaces contrast with the nanopillared surfaces by freezing at later times and therefore in larger drop sizes. For the plain surface, the larger the size of the droplet, the slower the direct growth of the condensed droplet.²³ The presence of non-condensable gases might reduce the net driving force or thermal gradient to mass transfer by adding a diffusion resistance to the vapor-air boundary layer.^{35,36} It limits the size of the growing droplet over a longer time of condensation and delays ice bridging time due to a larger void between the just formed ice nuclei and the neighboring evaporating droplet as shown in Figs. 2(d) and 4(d). The droplets are also cloudy and white when the surfaces finish freezing and expand considerably [see supplementary material, Sec. IV(C), VIII (b)-(c)].

The "final freezing time", is defined as the moment when all the droplets on entire surface under the microscope have frozen. To account for any inconsistencies, all tests on a surface were performed under same conditions. At 40% RH, the nanopillared surface has an average final freezing time of 73.6 s, ranging from 46 s to 124 s [Fig. 3, see supplementary material, Sec. III (a)-(b)]. The standard deviation is 17.3 s, and the coefficient of variance is 23.5%. At 40% RH, the average freezing time for the plain surface is 369.5 s. However, the Teflon© coated surface has an average final freezing time

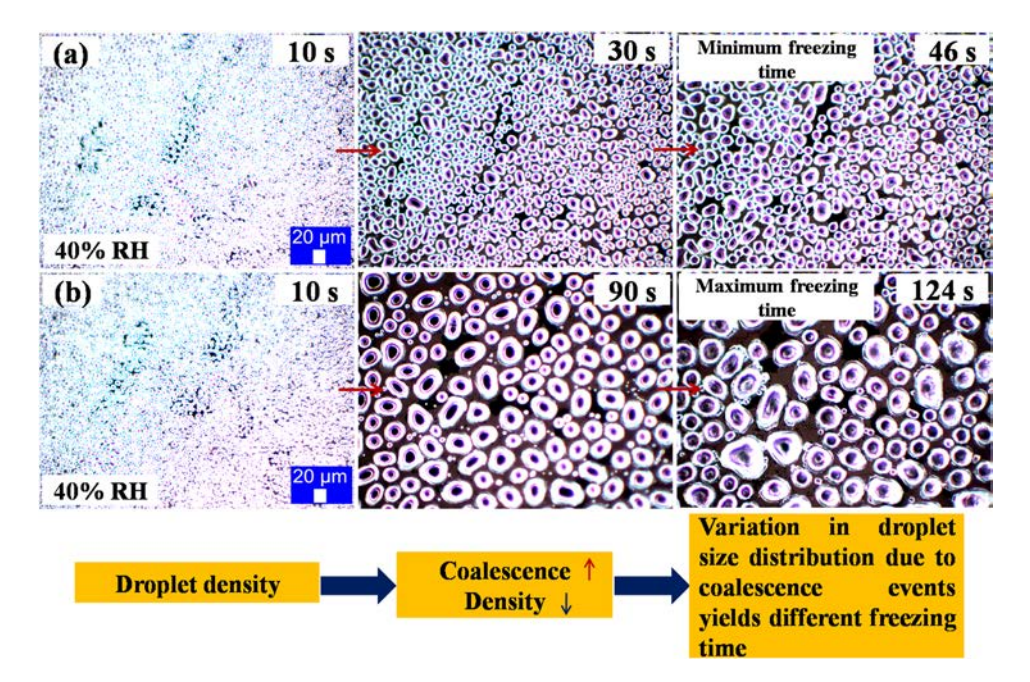


FIG. 3. Images of the (a) minimum and (b) maximum freezing time for two different trials on nanopillar surface at 40% RH [see supplementary material, Sec. III (a)-(b)].

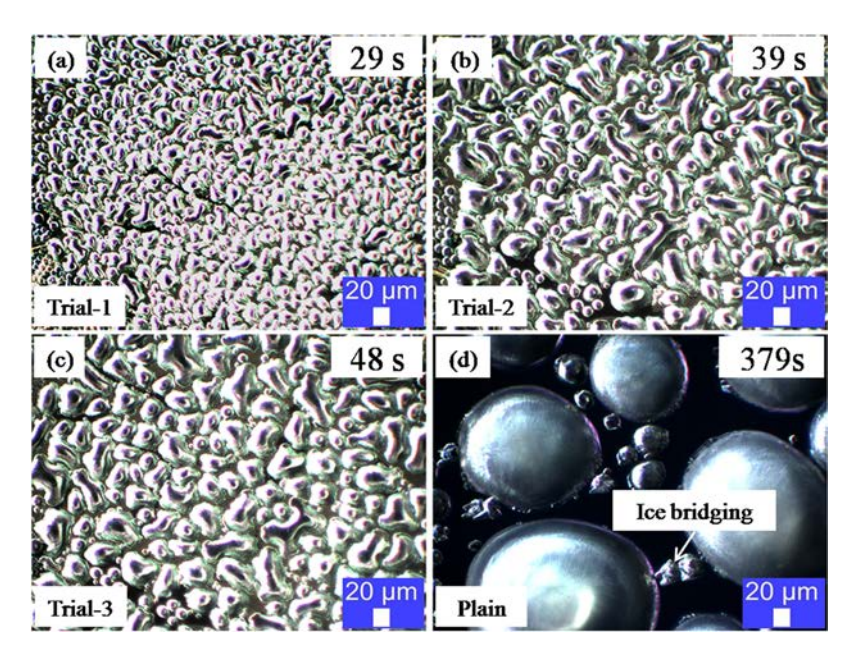


FIG. 4. Images taken when the surface fully freezes for 60% relative humidity (a) nanopillars frozen at 29 s, (b) nanopillars frozen at 39 s, (c) nanopillars frozen at 48 s, and (d) plain surface frozen at 379 s. (a), (b), and (c) are different trials on the same nanopillared surface.

of 721.75 s. Due to the increase of the local nucleation energy barrier, the coated surface increases the average freezing time compared to the plain surface. At 60% RH, the nanopillared surface has an average freezing time of 34.5 s, ranging from 13 s to 57 s. The standard deviation is 11.6 s, and the coefficient of variation is 22.6%. At this humidity, the average freezing time for a plain surface is 414.0 s. As it can be seen in the boxplots in Fig. 5, the 60% RH nanopillared surface tends to freeze faster than the 40% RH surface, with a few outliers, and both nanopillared surfaces freeze faster than a plain surface.

The "onset of freezing" is defined as the time when the first drops in the view of the microscope freeze. This happens due to the ice bridge invading just outside the view of the microscope. The delta freezing time is the difference between the "onset of freezing time" and the "final freezing time" (see supplementary material, Sec. VIII). The 40% RH nanopillar surface has an average delta freezing time of 11.7 s, ranging from 7 s to 21 s. The standard deviation for this surface and relative humidity is 3.7 s, with a coefficient of variance of 31.9%. The plain surface at these conditions has an average delta freezing time of 36.0 s. Teflon© coated surface has an average delta freezing time of 86.5 s, ranging from 67 s to 94 s (see supplementary material, Sec. VI). At 60% RH, the nanopillared surface has the average delta freezing time of 2.6 s, varies from 1 s to 8 s. The standard deviation is 1.3 s,

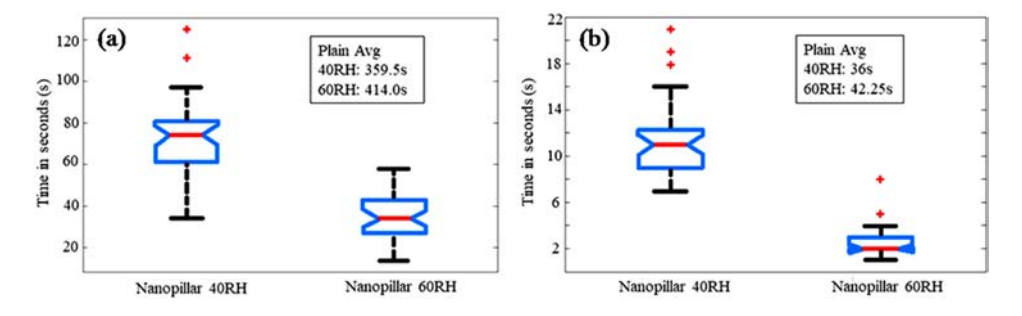


FIG. 5. (a) A boxplot for the freezing times of the nanopillared surface at 40% RH and 60% RH (b) a boxplot for the delta freezing time of the nanopillared surface at 40% RH and 60% RH.

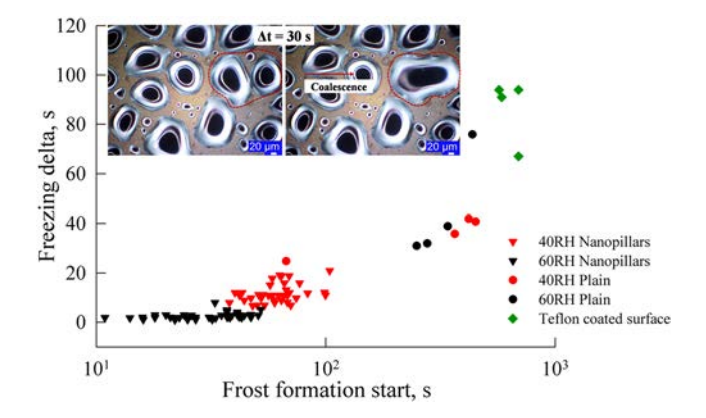


FIG. 6. Relationship between the start of frost formation and the freezing delta time for both plain and nanopillared surfaces at both 40% RH and 60% RH. The data for Teflon© coated surface at 35% RH has also been presented for the comparison. The inset images show the coalescence of droplets on nanopillared surface in a period of 30 seconds at 40% RH.

and the coefficient of variance is 51.8%. In comparison, the average delta freezing time for the plain surface at this relative humidity is 42.2 s.

As it can be seen in Fig. 5, the delta freezing time for the 60% RH nanopillar surface tends to be less than the 40% RH surface, and both are less than their corresponding plain surfaces. Furthermore, in Fig. 6 it is also observed that, the beginning freezing time (frost formation start), and freezing delta appears to be proportionately related for all of the surfaces.

In summary, nanopillared surfaces significantly accelerate freezing. At 60% RH, the average freezing time of a nanopillared surface (34.5 s) is an order of magnitude faster than a plain hydrophilic surface (414.0 s). Droplets are pinned by the pillars. The pinning effect decreases the frequency of coalescence events. This significantly prevents droplet growth. Freezing on nanopillared surfaces showed strong statistical variations. Analysis of this data elucidated a relationship between the "onset of freezing" and the "freezing propagation rate" for the considered nanopillar surface. The sooner the surface begins the onset of freezing, the faster the propagation of freezing will be. In the initial nucleation stages droplets are numerous and tightly packed on the surface. Over time, if condensation continues, droplets will merge and create larger voids between droplets. These larger voids may require ice bridging to propagate the freezing front. The relationship between the "onset of freezing" and "final freezing time" provides valuable insight into the design of engineered surface such as nanopillared surface for controlling condensate freezing.

See supplementary material for additional information regarding the MPL process, contact angle measurement (Section I), experimental setup (Section II), videos showing the minimum and maximum freezing times at 40% RH on nanopillar surfaces [Section III (a)-(b)], identification of the frozen droplet (Section IV), initial nucleation density for plain and nanopillared surface at 60% RH (Section V, Video V), the freezing dynamics and times for Teflon[©] coated surface (Section VI, Video VI), droplet size distribution at minimum, average, and maximum freezing times on nanopillar and at one of the trials on the plain surface (Section VII), and estimation of the freezing delta (Section VIII) have also been provided.

This material is based upon work supported by the US National Science Foundation under Grant No. 1604183 and 1653792. The authors would like to thank Dr. Steven Eckels and the Institute for Environmental Research (IER) for the use of their environmental chambers. We would also like to thank Cara Snyder for her initial experiments which eventually led to this work.

¹ J. B. Borevko and C. P. Collier, ACS Nano 7(2), 1618–1627 (2013).

² A. S. Van Dyke, D. Collard, M. M. Derby, and A. R. Betz, Applied Physics Letters 107(14), 141602 (2015).

³ Y. Zhang, M. R. Klittich, M. Gao, and A. Dhinojwala, ACS Applied Materials & Interfaces 9(7), 6512–6519 (2017).

⁴ Y. Chen, P. Lu, C. Shen, and Q. Zhang, Applied Thermal Engineering 90, 86–93 (2015).

⁵ K. Kim and K.-S. Lee, International Journal of Heat and Mass Transfer **60**, 505–511 (2013).

⁶ M. He, J. Wang, H. Li, X. Jin, J. Wang, B. Liu, and Y. Song, Soft Matter **6**(11), 2396–2399 (2010).

⁷ Y. Zhao and C. Yang, Applied Physics Letters **108**(6), 061605 (2016).

- ⁹ D. P. Singh and J. P. Singh, Applied Physics Letters **102**(24), 243112 (2013).
- ¹⁰ S. Wang, W. Zhang, X. Yu, C. Liang, and Y. Zhang, Scientific Reports 7, 40300 (2017).
- 11 Z. J. Wang, D.-J. Kwon, K. L. DeVries, and J.-M. Park, Experimental Thermal and Fluid Science 60, 132-137 (2015).
- ¹² J. B. Boreyko, R. R. Hansen, K. R. Murphy, S. Nath, S. T. Retterer, and C. P. Collier, Scientific Reports 6 (2016).
- ¹³ C. Stamatopoulos, J. Hemrle, D. Wang, and D. Poulikakos, ACS Applied Materials & Interfaces 9(11), 10233–10242 (2017).
- ¹⁴ Q. Ma, X. Wu, F. Chu, and B. Zhu, Applied Thermal Engineering **138**, 627–632 (2018).
- ¹⁵ D. Attinger, C. Frankiewicz, A. R. Betz, T. M. Schutzius, R. Ganguly, A. Das, C.-J. Kim, and C. M. Megaridis, MRS Energy & Sustainability-A Review Journal, 1, E4, (2014).
- ¹⁶ S. Chavan, D. Park, N. Singla, P. Sokalski, K. Boyina, and N. Miljkovic, Langmuir **34**(22), 6636–6644 (2018).
- ¹⁷ B. Li and D.-W. Sun, Journal of Food Engineering **55**(3), 277–282 (2002).
- ¹⁸ L. Zheng and D.-W. Sun, Trends in Food Science & Technology 17(1), 16–23 (2006).
- ¹⁹ H. Kiani and D.-W. Sun, Trends in Food Science & Technology 22(8), 407–426 (2011).
- ²⁰ E. Alizadeh, N. Chapleau, M. De Lamballerie, and A. Le-Bail, Innovative Food Science & Emerging Technologies 8(4), 493–499 (2007).
- ²¹ M. N. Martino, L. Otero, P. Sanz, and N. Zaritzky, Meat Science **50**(3), 303–313 (1998).
- ²² B. Li and D. W. Sun, Journal of Food Engineering **54**(3), 175–182 (2002).
- ²³ M. R. Haque, C. Qu, E. C. Kinzel, and A. R. Betz, Nanoscale and Microscale Thermophysical Engineering 22(4), 270–295 (2018).
- ²⁴ C. Qu and E. C. Kinzel, Optics Letters **41**(15), 3399–3402 (2016).
- ²⁵ A. Bonakdar, M. Rezaei, R. L. Brown, V. Fathipour, E. Dexheimer, S. J. Jang, and H. Mohseni, Optics Letters 40(11), 2537–2540 (2015).
- ²⁶ O. Shavdina, L. Berthod, T. Kampfe, S. Reynaud, C. Veillas, I. Verrier, M. Langlet, F. Vocanson, P. Fugier, and Y. Jourlin, Langmuir 31(28), 7877–7884 (2015).
- ²⁷ J. C. Hulteen and R. P. Van Duyne, Journal of Vacuum Science & Technology A: Vacuum, Surfaces, and Films 13(3), 1553–1558 (1995).
- ²⁸ R. Enright, N. Miljkovic, A. Al-Obeidi, C. V. Thompson, and E. N. Wang, Langmuir **28**(40), 14424–14432 (2012).
- ²⁹ R. Wen, Z. Lan, B. Peng, W. Xu, R. Yang, and X. Ma, ACS Applied Materials & Interfaces 9(15), 13770–13777 (2017).
- ³⁰ J. E. Castillo, J. A. Weibel, and S. V. Garimella, International Journal of Heat and Mass Transfer 80, 759–766 (2015).
- ³¹ Q. Zeng and S. Xu, The Journal of Physical Chemistry C **119**(49), 27426–27433 (2015).
- ³² S. Nath, S. F. Ahmadi, and J. B. Boreyko, Nanoscale and Microscale Thermophysical Engineering 21(2), 81–101 (2017).
- ³³ R. N. Bohm, A. R. Betz and E. Kinzel, presented at the ASTFE Digital Library, 2017 (published).
- ³⁴ M. R. Haque and A. R. Betz, presented at the ASME 2018 16th International Conference on Nanochannels, Microchannels, and Minichannels, 2018 (published)..
- ³⁵ R. Enright, N. Miljkovic, N. Dou, Y. Nam, and E. N. Wang, Journal of Heat Transfer 135(9), 091304 (2013).
- ³⁶ A. Ghosh, S. Beaini, B. J. Zhang, R. Ganguly, and C. M. Megaridis, Langmuir **30**(43), 13103–13115 (2014).